Multifunctional Fluorinated Copolymer Nanoparticles via a Cationic Dendritic-Based Macromolecular RAFT-CTA

*Anuja Kulkarni, Mahesh Loku Yaddehige, Daniel J. Cooke, Christine M. Hamadani, Alex S. Flynt, Eden E. L. Tanner, Emily L. Que, and Davita L. Watkins**

As the field of theranostics expands, an imminent need arises for multifaceted polymer-based nanotechnologies for clinical application. In this work, reversible addition-fragmentation chain transfer (RAFT) aqueous emulsion polymerization is used to form ^{19}F-containing amphiphilic hybrid block copolymers (HBCs). Employing a cationic dendritic macromolecular chain transfer agent (mCTA), polymer frameworks comprised of chemically distinctive blocks of differing architectures (i.e., dendritic and grafted/linear) are strategically designed and synthesized. In aqueous media, self-assembled polymer nanoparticles (PNPs) are formed. Their physicochemical properties and their potential as biomaterials for MRI applications are assessed. By showcasing a newly established mCTA and using these resulting PNPs as imaging probes, the work expands the design space of RAFT polymerization in biomedical research, paving the way for the development of more effective and versatile MRI imaging tools.

1. Introduction

Magnetic resonance imaging (MRI) has revolutionized the field of diagnostics. It has proven to be a powerful tool that produces high-quality images of living tissue, all while being a noninvasive imaging technique that allows for the assessment of anatomic and physiological processes.[1–3] In clinical settings, MRI is primarily used to visualize the spatial biodistribution of hydrogen atoms, mainly in water and lipid molecules. Paramagnetic contrast agents, such as chelates of Gd^{3+}, Fe^{3+}, or Mn^{2+}, are often introduced as contrast agents to enhance imaging. These agents function by reducing the relaxation times of local ^{1}H nuclei through magnetic interactions between unpaired electrons and hydrogen nuclei.[4] This localized change in contrast aids in differentiating between healthy and diseased tissue and further highlights the unique power of MRI as a diagnostic tool.

Despite the significant advancements in MRI contrast agents, these technologies still face numerous limitations. The high background signal from intrinsic sources of contrast, specifically water, in tissue often poses challenges in distinguishing diseased tissue using ^{1}H relaxation agents.[5] This is because detection is primarily contrast-induced and based on indirect modulation of nearby nuclei. An alternative approach involves directly monitoring the nuclear spins of the contrast agent rather than the neighboring spins, affording quantitative measurement of the local concentration of the contrast agents. However, this approach is impractical when observing ^{1}H spins due to the overwhelming signal from endogenous protons in the body. Such limitations have unlocked avenues for the development of biocompatible contrast agents containing biologically rare yet magnetically active nuclei such as ^{19}F, ^{23}Na, and ^{31}P. Of these emerging contrast agents, materials based on the ^{19}F isotope appear to be the most promising.[6] Comparable to ^{1}H, the ^{19}F isotope has a 100% natural abundance and nuclear spin (I) of ½. The gyromagnetic ratio of ^{19}F is similar to hydrogen (40.08 vs 42.58 MHz T^{-1} of ^{1}H),[7] meaning that the ^{19}F atoms can be successfully imaged by standard ^{1}H MRI techniques, requiring minor tuning of the radio-frequency and allowing simultaneous imaging of both ^{1}H and ^{19}F signals, if needed.[8] Uniquely, ^{19}F chemical shifts are varied in a broad range (>350 ppm) and only biologically abundant in trace quantities ($<10^{-6}$ M), rendering highly discrete imaging profiles. It has a Van der Waals radius of 1.47 Å, making it larger than the hydrogen atom (1.20 Å).[9] Interestingly, when incorporated into a polymeric framework, novel behaviors have been observed,

A. Kulkarni, D. L. Watkins
Department of Chemistry and Biochemistry
The Ohio State University
Columbus, OH 43210, USA
E-mail: watkins.891@osu.edu

M. L. Yaddehige, C. M. Hamadani, E. E. L. Tanner, D. L. Watkins
Department of Chemistry and Biochemistry
University of Mississippi University
Oxford, MS 38677, USA

D. J. Cooke, E. L. Que
Department of Chemistry
University of Texas at Austin
Austin, TX 78712, USA

A. S. Flynt
Center for Molecular and Cellular Biosciences
University of Southern Mississippi
Hattiesburg, MS 39406, USA

D. L. Watkins
William G. Lowrie Department of Chemical and Biomolecular Engineering
The Ohio State University
151 W Woodruff Ave., Columbus, OH 43210, USA

The ORCID identification number(s) for the author(s) of this article can be found under https://doi.org/10.1002/macp.202400354

DOI: 10.1002/macp.202400354

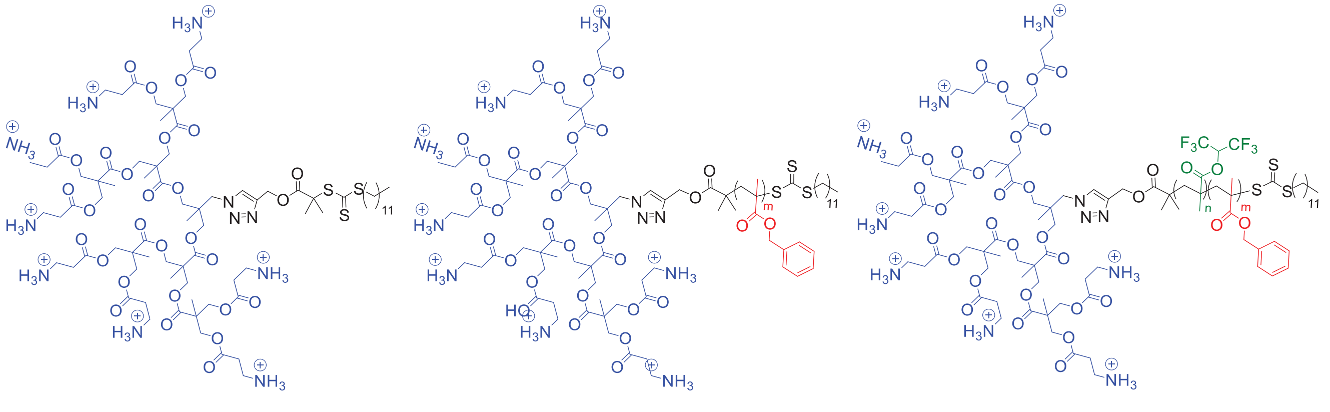

mCTA-8ala

pBzMA-NH$_3$+

pBz_HF

Figure 1. mCTA(Mcta-8ala, and polymers of interests:pBzMA-NH$_3^+$ and pBz_HF; variation of HFMA affords P(Bz_HF_5), P(Bz_HF_10), and P(Bz_HF_20).

presumably due to the high electronegativity, high ionization potential, and low polarizability of the fluorine atom.[10–12]

Despite its undeniable potential, ^{19}F MRI is still underutilized, primarily due to toxicity issues, low fluorine molecular content, water-solubility, and often unfavorable physical/biological properties.[13–15] Consequently, the development of new ^{19}F MRI contrast agents are an ongoing challenge and critical need in biomedical diagnostic research. Herein, we report the use of reversible addition-fragmentation chain transfer (RAFT) aqueous emulsion polymerization to form ^{19}F-containing amphiphilic hybrid block copolymers (HBCs). Designed as a customizable, multifunctional platform for biomedical applications, the hierarchical structure of these polymers allows for more sophisticated control over biological interactions compared to conventional linear RAFT-synthesized polymers. Studies have shown that amphiphilic polymers with distinct chemical blocks have the ability to encapsulate drugs more efficiently and provide better control over drug release.[16–18] These properties make these polymers particularly attractive for advanced biomedical applications.

Employing a cationic dendritic macromolecular chain transfer agent (mCTA), unique polymer frameworks comprised of chemically distinctive blocks of differing architectures (i.e., dendritic and grafted/linear) were strategically designed and synthesized (**Figure 1**). Upon reconstitution into aqueous media, the self-assembled polymer nanoparticles (PNPs) were formed and their potential as biomaterials for MRI applications was assessed. By using these PNPs as imaging probes, the work highlights several advantages over traditional imaging agents—specifically, the tunability of ^{19}F content, surface properties, and multicomponent domains yielding multifunctional contrast agents. This study exemplifies the effect of polymer topology on nanomaterial properties and expands the design space of RAFT polymerization in biomedical research.

2. Results And Discussion

2.1. Design and Synthesis

^{19}F MRI depends on the use of a fluorinated contrast agent. Applicable ^{19}F MRI contrast agents should satisfy several critical criteria, such as a single ^{19}F resonance peak for maximum sensitivity and minimum imaging artifacts, appreciable fluorine content for high sensitivity and low toxicity, sufficiently long spin–spin relaxation time (T_2), and high signal-to-noise ratio (SNR) for optimal image.[19–22] Here a cationic dendritic chain transfer agent (mCTA-8-ala) was designed and synthesized with the aim of producing a library of HBCs possessing a 13:87 hydrophilic to hydrophobic ratio capable of self-assembling into biomimetic vesicles. Inspired by Malkcoh's bisMPA dendron, a G1 dendron was synthesized and capped with alanine end-groups to yield an azide-cored dendron (bMPA). Copper-catalyzed alkyne-azide cycloaddition (CuAAC) between the dendron and S-dodecyl- S′-(α,α'-dimethyl-α''-propargyl ester) trithiocarbonate (DDPET) afforded the RAFT agent. The Boc groups were removed with trifluoroacetic acid (TFA), resulting in the trifluoroacetate salt of the cationic dendron, thus yielding an mCTA possessing a positively charged surface and enhanced water solubility.

Initial studies began with the chain extension and incorporation of immiscible monomer, benzyl methacrylate (BzMA). Notably, both the design and synthesis of the mCTA and its applicability are suitable for RAFT-mediated polymerization-induced self-assembly (PISA). However, here, we aim to showcase the versatility of a novel mCTA. For this proof-of-concept study, ≈13 kDa amphiphilic HBC comprised of a hydrophilic dendritic head, the mCTA, and a hydrophobic linear PBzMA block was desired. BzMA was selected as the monomer and hydrophobic segment due to its literature precedent in aqueous RAFT and favorable mechanical and self-assembling properties, including a glass transition temperature (Tg) that prevents assemblies from becoming kinetically trapped and ability to participate in π-π stacking interactions.[23,24] As a water-immiscible monomer, it has shown efficiency in RAFT aqueous emulsion polymerization, affording stable self-assembled nanostructures.[25] The water-soluble 2, 2′-azobis(2-methyl-propionamidine) dihydrochloride (V_{50}) was used as the initiator. The monomer to initiator ratio was fixed for this work as 5:1. A monomer: mCTA feed ratio of 50:1 was chosen to obtain an expected hydrophobic to hydrophilic weight ratio of 83:17. Upon addition of BzMA monomer to a solution of mCTA-8ala in DI water resulted in phase separation, but upon degassing, the solution turned turbid, suggesting that

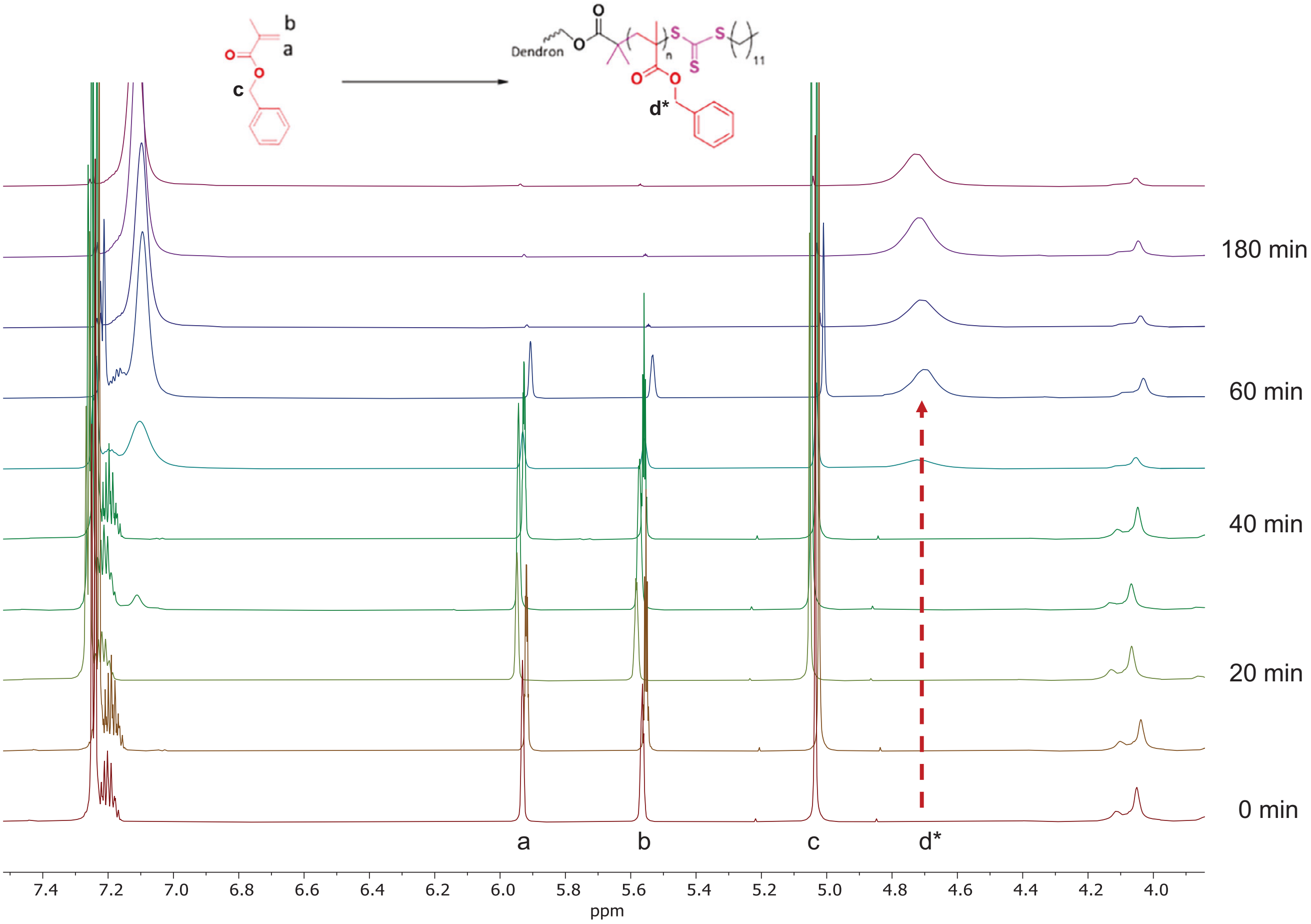

Figure 2. ^{1}H NMR spectra of the reaction of mCTA-8ala with BzMA to form pBzMA-NH$_3$$^+$.

mCTA-8ala may also act as an emulsion stabilizer. For this study, we found it imperative to maintain a low pH (≈5) as alanine-functionalized bMPA has been shown to be relatively unstable at neutral/basic pH at elevated temperatures. Given the pH sensitivity of this initiator, the pH of mCTA-8ala in water at a concentration of 0.37 M was maintained at ≈1.7. Monomer conversion was determined by ^{1}H NMR spectroscopy and the average degree of polymerization (DP) obtained was 77.6 with a molecular weight of 13.6 kDa corresponding to the hydrophobic to hydrophilic ratio of 88:12 differing from the calculated (83:17). We speculate that the higher value of DP and the discrepancy in the hydrophobic to hydrophilic ratio is due to incomplete CTA consumption in the reaction that has also been observed with previous reports.[26,27] Additionally, reports have shown that DDPET has shown suboptimal insertion for methacrylic monomers.[28] The synthesized polymers were analyzed using SEC. The shoulder peak in the SEC spectra confirmed the incomplete consumption of the CTA (Supporting Information). Sampling involved the dilution of each extracted aliquot of the reaction mixture into DMSO-d_6, which is a suitable solvent for both BzMA and pBzMA-NH$_3$+. **Figure 2** provides the monomer conversion versus time profile of BzMA with mCTA-8ala. ^{1}H NMR signals corresponding to the monomer (a – 6.10, b – 5.65, c – 5.28 ppm) and product (d* – 4.86 ppm) were monitored as the reaction progressed. Resonance signals a and b corresponding to the alkene of the BzMA decrease with time, and signal d* increases, showing the polymerization progress Figure 2.

The kinetics of the polymerization of BzMA was also monitored (**Figure 3**). Interestingly, the reaction of mCTA-8ala with BzMA exhibited a relatively short incubation period of ≈75 min, consisting of a 45–50 min nucleation period followed by a rapid

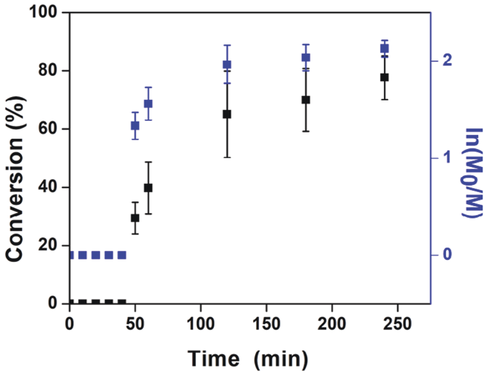

Figure 3. Monomer conversion versus time profile of pBzMA-NH$_3$$^+$ polymerization.

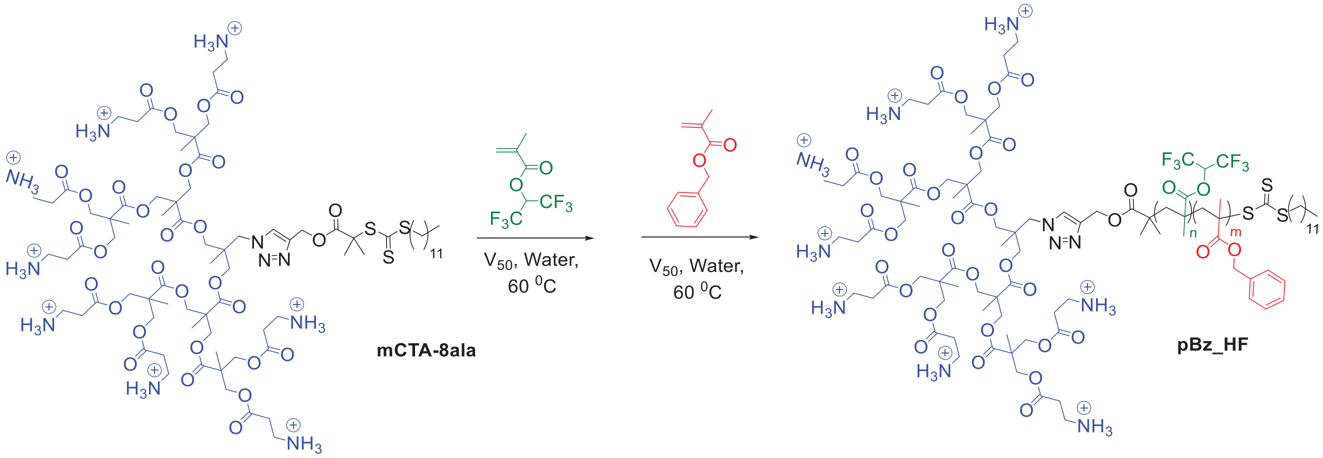

Figure 4. Synthetic route for the preparation of pBz_HF, n is the number of HFMA units, and m is the number of BzMA units. By changing HFMA (n) to BZMA (m) ratio (n:m) into 1:5, 1:10, and 1:20, we synthesized P(Bz_HF_5), P(Bz_HF_10), and P(Bz_HF_20).

rate enhancement. At 50 min, the DP obtained was of 30, which gradually increases to 40 for 60, 65 for 120, 70 for 180 min, and saturated kinetics is achieved after 240 min, indicating a DP of 77.6 for the PBzMA block and a polymerization that goes to >98% conversion within 4 h. The kinetics profile correlates well with conversion profiles commonly observed for aqueous RAFT emulsion polymerization, where micellar nucleation and localized concentration induce polymer formation.[29–31] However, a slight deviation from pseudo-first-order kinetics is observed. This variation is most likely due to the sterically hindered mCTA-8ala. Further studies are needed to optimize reaction conditions and assess the effects of the dendritic group on polymerization kinetics. Nonetheless, as a proof-of-concept study, mCTA-8ala displays promise as an RAFT agent for accessing hierarchical polymer structures.

The RAFT agent, mCTA-8ala, was then used to synthesize fluorinated HBCs, pBz_HF, using 1,1,1,3,3,3-hexafluoropropan-2-yl methacrylate (HFMA) and hydrophobic monomer BzMA. Note that a sequential synthesis was applied in which pHFMA was formed using mCTA-8ala to yield mCTA-8ala-pHF followed by a BzMA polymerization to afford pBz_HF. For this design, we sought to ensure that the fluorine amount was enough to achieve a well-defined MRI signal without exhibiting a cytotoxic response as a PNP. Additionally, the incorporation of the fluorinated monomer has been shown to result in higher conversion due to the electron-withdrawing nature of the fluorine atom.[32] A general synthetic scheme for the pBz_HF is shown in **Figure 4** to illustrate a library of fluorinated HBCs in which the HFMA (n) to BzMA (m) ratio (n:m) of 1:5, 1:10, and 1:20, resulted in P(Bz_HF_20), P(Bz_HF_10) and P(Bz_HF_5), respectively. The fluorinated block varied by 20, 10, and 5% while the pBzMA remained constant to stabilize the hydrophobic segment of the resulting PNP via π-π staking between phenyl groups.

The design and synthesis of the ^{19}F-containing amphiphilic HBCs were optimized to achieve a higher level of biocompatibility.[33,34] In this case, the target MW for the fluorinated HBCs was decreased by half (<10 kDa). The final products of the two-step sequential polymerization were confirmed by ^{1}H and ^{19}F NMR spectroscopy, as displayed in Figures S1–S10 (Supporting Information). ^{1}H NMR signals corresponding to the HFMA monomer (1.95, 6.25, and 6.04 ppm) were monitored as the reaction progressed. The resonance signals for the alkene (6.25 and 6.04 ppm) decreased over the course of the reactions while the methyl peak shifted from 1.89 to 0.9 ppm, indicating monomer consumption and completion of polymerization. ^{19}F NMR was conducted to confirm the absence of free HFMA monomer in the reaction mixture versus the presence of fluorinated polymer. ^{19}F NMR signals for the monomer appeared as a doublet peak at −72.8 ppm that broaden and shifted to −73.6 ppm as the reaction progressed (Figures S8–S10, Supporting Information). The molecular weight and the degree of polymerization (DP) were calculated using proton NMR spectra for all the polymers (**Table 1**). SEC was utilized to confirm the molecular weight and polydispersity of the polymers (Table 1; Figure S11, Supporting Information). The SEC displayed a nonbimodal peak, which confirmed the complete consumption of the CTA, and was not observed in the CTA BzMA reaction. It is speculated that the reactivity of the fluorinated monomer aids with the consumption of the CTA and facilitates the polymerization process.[32]

2.2. Self-Assembly And Morphology

Tabulation of PNP characteristics is provided in **Table 2**. The critical aggregation concentration (CAC) of the PNPs was evaluated

Table 1. Summary of polymerization results by aqueous RAFT emulsion polymerization, 25% (v/v), (M:CTA:I = 500:5:1 mol ratio).

Polymer	HF (n)$_{NMR}$	Bz (m)$_{NMR}$	Mn [g mol^{-1}]	Mw [g mol^{-1}]	Đ
P(HF_Bz_20)	2	43	5284	6973	1.32
P(HF_Bz_10)	4	39	8069	9804	1.22
P(HF_Bz_5)	8	40	6797	8079	1.19

M$_n$, M$_w$, Đ denote number average molar mass, weight average molar mass, and dispersity, respectively, Determined by DMF SEC using a series of poly (methyl methacrylate) (PMMA) calibration standards.

Table 2. CAC values, the average hydrodynamic diameter of the PNPs by TEM and DLS (intensity), and surface charge.

Polymer	CAC / [mg L^{-1}]	D_H^{DLS} /nm	PDI	D^{TEM} /nm	Nagg	ζ-potential [mV]
P(Bz_HF_20)	1.26 ± 0.45	165.2 ± 38.7	0.04	175.3	17	30.5 ± 4.8
P(Bz_HF_10)	11.22 ± 0.59	135.3 ± 34.1	0.05	154.2	18	31.1 ± 3.9
P(Bz_HF_5)	15.85 ± 1.32	191.0 ± 48.2	0.12	160.4	21	33.6 ± 3.9

using the pyrene probe method (Figures S12–S14, Supporting Information).[35] The CAC for the fluorinated polymers ranged from 1.26 to 15.85 mg L^{-1}, providing relatively low CAC values. These results are presumably due to the combined hydrophobicity and lipophobicity nature of the fluorinated compound, as well as the steric bulk of the hydrophilic dendron. Nonetheless, they are comparable to those found in the literature and correlate to the candidacy of these fluorinated PNPs as potential biomaterials. As the three polymers have the same hydrophobic segment yet varying amounts of fluorine content, CAC values were determined and were shown to increase with the fluorine amount. P(Bz_HF_5), which has the highest amount of fluorine, has the highest CAC value (15.85 mg L^{-1}), and P(Bz_HF_20), which has the lowest amount of fluorine, has the lowest CAC value (1.26 mg L^{-1}), with the P(Bz_HF_10) having an intermediate CAC value of 11.22 mg L^{-1}. Consequently, it appears that having a higher fluorine amount leads to a higher CAC value. Ideally, a low CAC value illustrates a more stable nanoaggregate and a resistance to dissociation upon dilution in the blood.[36,37] Based on CAC values, the results indicate that P(Bz_HF_20) forms more stable PNPs compared to P(Bz_HF_5) and P(Bz_HF_10).

An aggregation number (N_{agg}) explains the average number of individual polymer units present in a spherical nanoaggregate once the CAC has been reached. N_{agg} is essential in this study because it affords the average fluorine percentage inside a PNP. P(Bz_HF_5), P(Bz_HF_10), and P(Bz_HF_20) have N_{agg} of 21, 18, and 17, respectively. The fluorescence quenching technique was carried out to calculate the N_{agg} of the PNPs. This technique is based on the quenching of pyrene fluorescence by a hydrophobic benzophenone quencher (Figures S15–S17, Supporting Information).[38]

The particle size of the dendritic aggregates in aqueous media was studied by DLS, which provides an estimate of the particle size as its hydrodynamic diameter. P(Bz_HF_5) has the largest particle size with an intensity average diameter of 191.0 ± 48.2 nm, with 0.12 PDI (Figures S18–S26, Supporting Information). PNPs formulated from P(Bz_HF_10) have an intensity average diameter 135.3 ± 34.1 nm, with 0.05 PDI. While PNPs achieved from P(Bz_HF_20) show an intensity average diameter of 165.2 ± 38.7 nm with 0.04. Based on the PDI value, all three PNPs show a narrow distribution of monodisperse PDI values below 0.2.[39]

To examine the morphology of the aggregates and support the particle size data obtained by the DLS, TEM analysis was conducted. TEM analysis indicated PNPs of P(Bz_HF_20), P(Bz_HF_10), and P(Bz_HF_5) as uniform monodispersed spherical aggregates (**Figure 5**) with an average particle size of 175.3, 154.2, and 160.4 nm, respectively. Overall, particle size analysis indicates that all three PNPs produce particles within an appropriate size distribution for cellular uptake.[40] All particle sizes are below 200 nm, which indicates that they can escape physiological barriers and possess the potential for prolonged circulation, therefore potentially reducing imminent clearance by the liver and spleen.[41,42]

The surface charge is significant for the stability of the PNPs in suspension and contributes to the adsorption of particles onto the cell membrane. Studies have shown the ability of cationic PNPs to stay in a tumor for a prolonged time due to favorable electrostatic interactions that can be made between the cationic PNP and the negatively charged cell membrane at the stage of cellular uptake.[43] After the adsorption of particles, the endocytic uptake rate depends on the particle size. Additional factors such as cell type, cellular uptake mechanism, and intracellular localization are taken into account when assessing the surface properties of PNPs and their potential application.[44] Nanoparticle surface charge is commonly expressed as a zeta potential, which is measured by the laser Doppler electrophoresis technique. P(Bz_HF_20), P(Bz_HF_10), and P(Bz_HF_5) have zeta potentials of 30.5 ± 4.8 , 31.1 ± 3.9, and 33.6 ± 3.9 mV, respectively. Generally, particles with positive surface charges above 15 mV display ideal properties such as higher tumor uptake and retention, decreased macrophage uptake (i.e., reduced unfavorable immune response), and longer particle circulation time.[45,46] The surface charge values for P(Bz_HF) PNPs are higher than the standard 15 mV due to the cationic surface. Additionally, the values amongst the PNPs are similar, indicating the surface charge is independent of fluorine content for the three polymers.

2.3. Cytotoxicity

It is essential to evaluate the cytotoxicity of the PNPs to see their potential as a nanocarrier. After physicochemical characterization, we evaluated the effects of PNPs on cell viability in HEK cells using the Lactate Dehydrogenase (LDH) assay (**Figure 6**). LDH is a cytosolic enzyme that catalyzes the interconversion between pyruvate and lactate.[47] If there is cell death, LDH will be released into growth media, which can be detected with a colorimetric assay. HEK cells were selected as a representation of human cell-nanoparticle interactions.

Among the three PNPs, P(Bz_HF_10) showed the least cytotoxicity (Figure 6; Figure S27, Supporting Information). At 0.2 μg mL^{-1}, an increase in cytotoxicity was observed compared to other higher concentrations. It is essential to note that 0.2 μg mL^{-1} is below the CAC value; thus, at this concentration, there is no PNP formation, only unimer or "free" polymer. From 1 to 125 μg mL^{-1}, cytotoxicity increases with the concentration. P(Bz-HF_5), which has the highest amount of fluorine, shows the highest cytotoxicity at a concentration between 1 and 25 μg mL^{-1}. At 125 μg mL^{-1} concentration, P(Bz-HF_20) shows the highest cytotoxicity, only 1.5% compared to P(Bz_HF_5). Overall, the observed cell cytotoxicity for the three PNPs was < 5%, which indicates P(Bz_HF) PNPs are generally non-toxic to living human cells (Figure 6; Figure S27, Supporting Information).

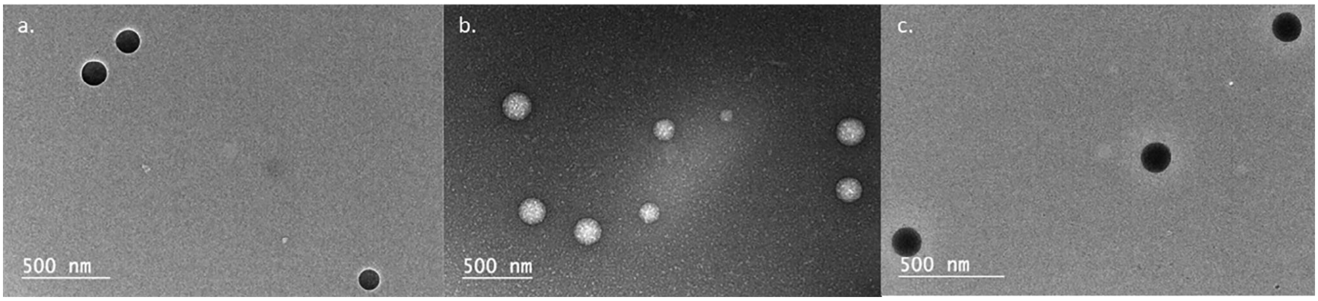

Figure 5. Nanoparticles formed by (a) P(Bz_HF_20), (b) P(Bz_HF_10), and (c) P(Bz_HF_5) under TEM.

Additionally, the intravenous (IV) biocompatibility of the P(Bz_HF) PNPs was measured via hemolysis assay on mouse red blood cells (Figure S28, Supporting Information). A nonionic detergent, Triton-X, was the positive control, and PBS was the negative control for the hemolysis assay. One-way ANOVA showed a significant difference between all three treatment groups ($p = 2.9\times10^{-13}$), with P(Bz_HF_20) inducing the highest RBC hemolysis (59.4 ± 0.8%). In comparison with P(Bz_HF_20), P(Bz_HF_10) and P(Bz_HF_5) show proportionally lower RBC hemolysis of 19.9 ± 0.5% ($p = 0.00004$) and 7.0 ± 0.1% ($p = 8.6\times10^{-6}$), demonstrating a significant correlation between HFMA:BZMA ratio and hemobiocompatibility which should be considered when considering nanoformulation and dosage for in vivo applications. Some degree of hemolysis is expected due to the positive charge of the PNP driving an interaction with the negatively charged RBC membrane. Interestingly, the PNP with the most positive surface charge and the highest relative amount of fluorine, P(Bz_HF_5), showed minimal hemolysis, acceptable for in vivo applications. Considering the relative similarity in size and zeta potential among the series, we hypothesize that the decrease in hemolysis seen for this polymer may be due to increased interactions between the terminal amine groups and the electronegative fluorine atoms, which may then reduce potential interactions with the RBC membrane, thereby reducing hemolysis. Additional surface modifications of the PNPs will be considered in future studies to further reduce the degree of hemolysis.

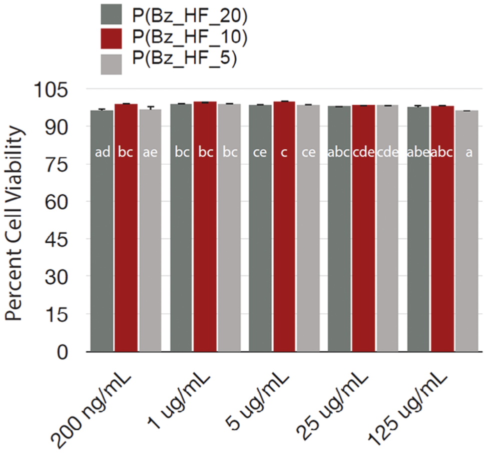

Figure 6. Cell viability after treatment with PNPs. The LDH assay determined cytotoxicity (percentage). Error bars denote the standard error, while letter denotes significance groups as determined by Tukey HSD ($p \leq 0.05$).

2.4. Relaxation Times (T_1/T_2)

In order to evaluate their potential as ^{19}F MRI contrast agents, the fluorinated PNPs were examined by ^{19}F NMR (470 MHz, 25 °C). Samples were dispersed in H_2O/D_2O (90/10, v/v). As displayed in Figures S29–S31 (Supporting Information), only one resonance signal was observed in each spectrum possessing a peak width of ≈6 Hz, confirming a single ^{19}F chemical environment in the PNPs. The ^{19}F NMR relaxation times spin-lattice (T_1) and spin–spin (T_2) of the PNPs were measured and listed in **Table 3**.

The spin−spin relaxation time T_2 is an important parameter determining the resultant MRI performance. A longer T_2 relaxation time is vital for producing intense ^{19}F MRI signals. T_2 relaxation usually proceeds more rapidly than T_1 recovery, and different biological tissues have different T_1 and T_2. For example, fluids have the longest T_1 and T_2; water-based tissues (T_1,1500–2000 ms and T_2, 40–200 ms range), while fat-based tissues are in the lower (T_1, 400–1200 ms range and T_2, 10–100 ms) range. In general, long T_2 values are preferred to avoid signal intensity loss, whereas short T_1 values are important to reduce acquisition times and increase the number of scans per unit time. For the T_1, relaxation times ranged from 2543 to 2750 ms, and T_2 relaxation times ranged from 634 to 1450 ms. P(Bz_HF_5) shows the shortest T_2 relaxation time, and P(Bz_HF_10) shows the highest T_1 relaxation time. Relaxation times were found to be much higher than the average of reported values, which is most likely a consequence of the sequential polymer synthesis, which results in limited flexibility of the fluorine moieties upon aggregation and PNP formation.[12,48] The MRI intensity (or signal-to-noise ratio, SNR) was found to be linearly dependent on the concentration of polymers (Figures S32–S34, Supporting Information): 5.1, 7.0,

Table 3. NMR relaxation times of the fluorinated PNPs in D_2O at 10 mg mL^{-1} concentration. Relaxation times showed appreciable change as a function of concentration (Supporting Information).

Polymer	T_1 / ms	T_2 / ms
P(HF_Bz_20)	2695	946
P(HF_Bz_10)	2750	1450
P(HF_Bz_5)	2543	634

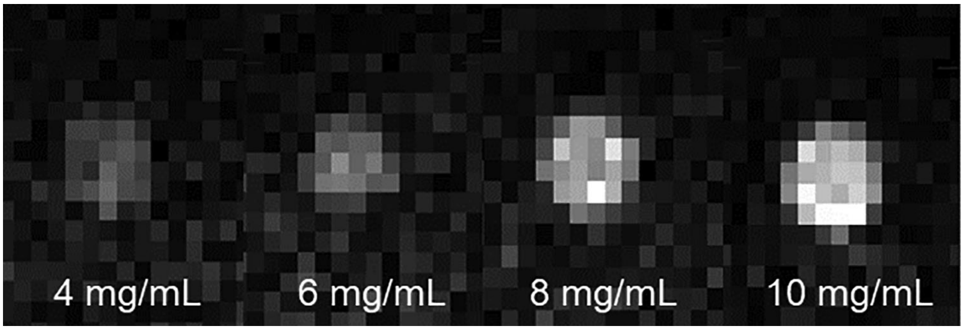

Figure 7. ^{19}F MRI phantom image of P(Bz_HF_10) at various concentrations: 4 (0.1 ^{19}F), 6 (0.15 ^{19}F), 8 (0.2 ^{19}F), and 10 (0.25 ^{19}F) mg mL^{-1}.

9.0, 11.8 for 4, 6, 8, and 10 mg mL^{-1}, respectively, and are higher relative to SNR values reported for high-resolution MRI.[49,50]

Based on the results of T_1 and T_2 measurements, P(Bz_HF_10) was selected for further evaluation. Using the N_{agg}, the concentration of ^{19}F was found to be 0.25 mg mL^{-1} for a 10 mg mL^{-1} PNP solution of P(Bz_HF_10). The limit of detection and image quality were assessed via ^{19}F MRI phantom images. PNP solutions of varying concentrations (4, 6, 8, and 10 mg mL^{-1}) were studied, and images were acquired over 30 min. A linear dependent intensity gradient can be observed throughout the samples, with the lowest concentration still being visible at 4 mg mL^{-1}. Although phantom images (**Figure 7**) provide sufficient contrast at varying concentrations, they highlight how closely packed the ^{19}F moieties are within the self-assembled PNPs and the effect it has on the MRI signal intensity. Here, the signal quality is attributed to the position and rigid conformation of the ^{19}F moieties within the polymer framework and resulting PNPs. The lack of flexibility and distribution reduces signal quality.[51,52] In turn, additional studies involving both monomer design and polymer composition will need to be conducted to increase the mobility of the ^{19}F moieties upon aggregation.

2.5. Encapsulation Studies and Cellular Uptake

In order to assess the potential of a secondary imaging agent and hydrophobic loading ability, encapsulation studies were conducted with a hydrophobic cyanine-based photothermal imaging agent, C3 (Figure S35, Supporting Information).[53,54] Cyanine-based dyes are generally used as imaging agents for photoacoustic and near-infrared fluorescence imaging. They can transform absorbed near-infrared (NIR) photons to heat as a photothermal agent and lower energy NIR photons for an image-guided combinatorial phototherapeutic agent. However, the application of cyanine dyes is limited due to solubility and instability in aqueous media, which decreases their imaging and therapeutic potential.

Without the presence of fluorinated polymer, the dye was completely insoluble in water, forming a separate layer on the water surface. Upon using a thin-film method to encapsulate the dye, the polymer-dye nanoparticle solution turned transparent blue, indicating an enhanced solubility. The encapsulation of C3 was assessed in terms of loading (DL%) and encapsulation efficiency (EE%).[55] Despite an intense color change observed in the solution, the loading ability of the P(Bz_HF) PNPs was calculated and estimated to be moderately low, with values of <10%.[56] The reported DL% of P(Bz_HF_20), P(Bz_HF_10), and P(Bz_HF_5) was 8.96%, 8.12%, and 7.63%, respectively. The reported EE% of P(Bz_HF_20), P(Bz_HF_10), and P(Bz_HF_5) was 24.61%, 24.10%, and 20.65% respectively. Such values are commonly due to differences in the precipitation time of the desired cargo (i.e., C3 dye) and the HBC or variations in the aggregation behavior.[57] Nonetheless, these DL% and EE% values highlight the potential of uploading hydrophobic cargo and secondary imaging agents into fluorinated nanoparticles.

C3-loaded fluorinated PNPs were then assessed as potential biological imaging agents. C3 dye fluorescence was measured after trafficking into HEK cells (**Figure 8**). LysoTracker green, a fluorescent dye that stains acidic compartments in live cells, was used to track the distribution and accumulation of dye-loaded PNPs in the cellular organelles.[58,59] The overlapped fluorescence images of C3-loaded fluorinated PNPs and LysoTracker are provided in Figure 8. P(Bz_HF_20) shows efficient loading with some accumulation in lysosomes but generalized cell labeling, while P(Bz_HF_10) and P(Bz_HF_5) were found as aggregates amongst cells with a small percentage observed to be entering cells for P(Bz_HF_5) PNPs. The observation is somewhat surprising, given similarities in size, surface charge, and loading properties amongst the HBCs. Results indicated that amongst the PNPs within this reported series, those with the lowest fluorine content, i.e., P(Bz_HF_20), yield PNPs with more efficient cellular uptake in HEK cells.[60]

3. Conclusion

Here, we present the preparation of fluorinated HBCs using aqueous RAFT polymerization. A novel cationic mCTA was used to synthesize the amphiphilic self-assembling polymers, and their PNPs were evaluated for biorelevant applications. Electron microscopy (TEM) and light scattering (DLS) analyses indicated that the resulting nanoparticles exhibited sizes within the therapeutic window ranging from 120 to 180 nm with zeta-potential values ranging from 30.5 to 33.6 mV. PNPs exhibit a single resonance in the ^{19}F NMR spectrum; however, they produced considerably higher than average reported MRI relaxation times. Despite their advantageous chemical structure, ongoing studies are geared toward increasing the local motion of the fluorinated moiety both by monomer redesign and block sequence. For this optimization, a correlation between fluorine monomer dispersion and signal quality will be assessed, where solubilizing groups

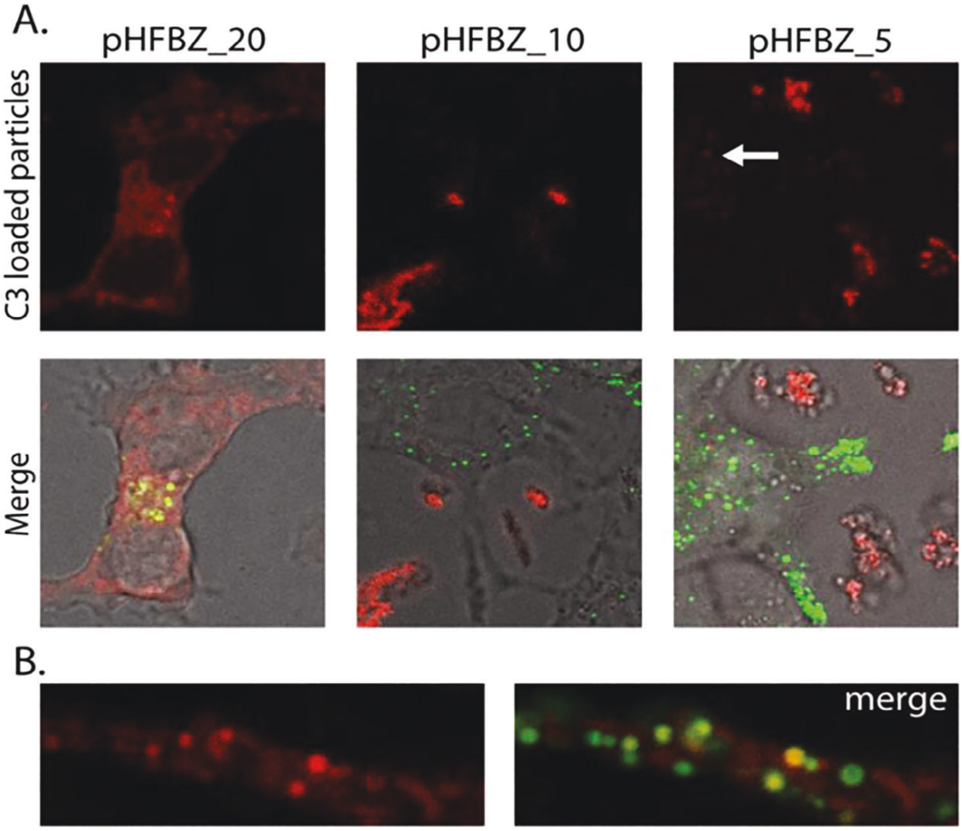

Figure 8. Cellular distribution of P(Bz_HF) derivates: A) imaging of C3 dye-loaded P(Bz_HF) PNPs. In HEK 293 cells: Top panels show C3 dye-loaded P(Bz_HF) fluorescence, bottom panel merge C3 dye-loaded P(Bz_HF) fluorescence (red), lysotracker green (green), and phase contrast. The white arrow shows C3 fluorescence on the interior of the cell. B) STED microscopy of cell filopodia showing C3 fluorescence (red) localized to lysosomes (green) and to presumptive endosomal bodies.

and copolymerization techniques employing mCTA-8ala as the RAFT agent will be done to improve fluorine distribution and signal quality. Notwithstanding, the reported PNPs show excellent promise, displaying minimal cell toxicity as well as the potential for dual imaging and therapy. The results of this work increase the availability of synthetic methods for multifunctional fluorinated materials and afford pathways toward building next-generation nanomaterials.

4. Experimental Section

Materials and Method: Common solvents, HPLC solvents, and reagents were purchased from commercial suppliers (Sigma–Aldrich and Fisher Scientific) and used without additional purification. Benzyl methacrylate (BzMA) and 1,1,1,3,3,3-hexafluoroisopropyl methacrylate (HFMA) were filtered through a small column of basic alumina before usage. Balb/C mouse blood was purchased from Bio-IVT (NY, USA).

^{1}H spectra were collected using a Bruker Avance 300 or 400 MHz spectrometer. Chemical shifts (δ) are denoted in parts per million (ppm) relative to an internal standard (tetramethyl silane-TMS) and referenced to a protonated solvent obtained from Cambridge Isotope Laboratories, Inc.

^{19}F NMR spectra were collected using a Bruker Avance 400 MHz spectrometer with H_2O/D_2O (90/10, v/v) as the solvent. Solution spectra were measured under the following measurement conditions: 90° pulse width 15 µs, relaxation delay 1 s, acquisition time 0.73, and 128 scans.

^{19}F spin–spin relaxation times (T_2) were measured using the Carr–Purcell–Meiboom–Gill (CPMG) pulse sequence at 298 K following a published protocol.[61] The samples were dissolved in H_2O/D_2O (90/10, v/v) at a concentration of 1–10 mg mL^{-1}. The 90° pulse was determined by dividing with a 360° pulse width, at which the NMR signal was zero. The relaxation delay was 1 s, and the number of scans was 64. Only values for the major peaks are reported. For each measurement, the echo times were from 2 to 770 ms, and 16 points were collected, which could be described by exponential functions for the calculation of T_2.

^{19}F spin–lattice (T_1) relaxation times were measured using the standard inversion–recovery pulse sequence. For each measurement, the relaxation delay was 2 s, and the number of scans was 32. Only values for the major peaks are reported. For each measurement, the recovery times were from 2 ms to 3 s, and 16 points were acquired. Values for the major peak at ≈−72.8 ppm are reported.

Size exclusion chromatography (SEC) measurements were done using DMF, and measurements were done at a flow rate of 0.8 mL min^{-1} at 55 °C. A Shimadzu 20A SEC system equipped with two PSS SDV analytical 1000 Å columns and a differential refractive index detector were used. The data was evaluated using Astra 7.0 software. The SEC system was calibrated using polymethylmethacrylate (PMMA) standards.

A JEOL 1230 TEM was used at 100 kV to obtain electron microscopy images using a bottom-mounted charge-coupled device (CCD) camera (Gatan Orius 831).

Additional experimental details can be found in the Supporting Information.

General Synthesis: The mCTA was prepared using a modified version of published work.[62–64] The mCTA, HFMA, V50, and water were added to a gas-tight conical vial and sonicated and incubated 1 h in a dark place. Then the solution was purged with Ar for 30 min and then the vial was placed in a 60 °C bath and monitored using NMR. After completion of polymerization, the polymer was purified by dialysis against Milli-Q water for 24 h and freeze-dried. Then the same RAFT polymerization method explained above was carried out with the BzMA. The final reaction mixture was purified using size exclusion chromatography (Sephadex LH-20) to obtain the pHFBz polymer systems.

Characterization of Polymers: The molar mass and the degree of polymerization (DP) were calculated using proton NMR spectra for all the polymers. DMSO-d_6 was used as the solvent, with TMS as the internal standard. ^{19}F NMR was carried out to confirm the absence of free HFMA monomer in the reaction mixture and the presence of fluorinated polymer. SEC was utilized to confirm the molar masses calculated by NMR and obtain the dispersity (Đ) of the polymers.

Preparation and Characterization of Nanoparticles: Polymer systems were formed into nanoparticles via a previously reported nanoprecipitation method.[57] 1 mg of the polymer was dissolved in THF (200 µL), and the resulting solution was added dropwise to a vial containing MilliQ water (2 mL) while sonicating. THF was allowed to evaporate under constant nitrogen flow. Nanoformulations were allowed to equilibrate for 12 h before testing.

Particle size and zeta potential (ζ-potential) measurements were carried out on a Zetasizer Nano ZS (Malvern Instrument) using a He–Ne laser (633 nm) detector angle of 173° at 25 °C. Concentration was kept 0.5 mg mL^{-1} for all the systems, and all measurements were done in triplicate to assure consistency. Morphologies of the nanoparticles were obtained by environmental TEM.

Critical Aggregation Concentration: For the measurement of the critical aggregation concentration (CAC), pyrene (1.7 mg, 8.41 µmol) was dissolved in 3 mL of acetone, and 40 µL of the solution was added to 40 mL of deionized water. A series of concentrations of the nanoaggregate suspension ranging from 10^{-8} to 10^{2} mg L^{-1} was prepared by dilutions of 2 mL per sample. Pyrene solution (2 mL) was added to each vial, and these solutions were equilibrated for 48 h in a dark area. The fluorescence spectra were obtained on a Varian Cary fluorometer from Agilent Technologies. An emission wavelength of 390 nm was used for pyrene, and the excitation spectra were recorded from 300 to 380 nm. The ratio of emission intensities at 338 and 333 nm was graphed as a function of the log of the concentration. The CAC was determined as the concentration at the intercept of the lines for the two linear regions of the obtained graphs.[35]

Determination of the Aggregation Number (N_{agg}): The fluorescence quenching technique was carried out to calculate the N_{agg} of the nanoparticles. This technique is based on the quenching of pyrene fluorescence by a hydrophobic benzophenone quencher.[38,65] N_{agg} was calculated by changing the quencher concentration using the following equation:

$$\ln\left(I_0/I\right) = \left[N_{agg}/\left(C_p - C_{CAC}\right)\right] \times C_q \tag{1}$$

where I_0 = fluorescence intensities of pyrene in the absence of quencher, I = fluorescence intensities of pyrene in the presence of quencher, C_p = molar concentration of the polymer, C_{CAC} = critical aggregation concentration and C_q = molar concentration of the quencher.

Encapsulation Studies: Chemical structures, absorbance, and emission profiles for each dye are given in the Supporting Information. 1 mg of C3 dye and 2 mg of the polymer were dissolved in THF (200 µL). The nanoprecipitation method stated above (preparation and characterization of nanoparticles) was followed to form dye-loaded nanoparticles. After the 12 h equilibrating period, the unloaded dye was filtered out using a 0.45 µm syringe filter. Water was then removed by freeze-drying. The resulting crude (dye-loaded nanoparticles) was re-dissolved in THF (10 mL) to solubilize the encapsulated dye. The amount of encapsulated dye was estimated using a Cary 6000 UV–vis spectrophotometer and a standard calibration curve obtained from free dye in THF. The encapsulation efficiency (EE%) and loading efficiency (DL%) were calculated for each dye using the following equations. M_C = mass of the dye in the nanoparticle, M_P = mass of LDBC, and M_{Ci} = mass of the dye initially added.[55,56]

In Vitro Cell Uptake and Cytotoxicity Assay: Human embryonic kidney (HEK293) cells were used for cytotoxicity assay. HEK cells were grown under the standard conditions (37 °C, 5% CO_2, DMEM media with 10% FBS). Then the nanoparticles were added to tissue culture media and allowed 24 h incubation period. A LysoTracker Green DND-26 (Invitrogen) staining was performed to image lysosomes simultaneously. The distribution of dyes in the cells was visualized with a laser scanning confocal and super-resolution microscopy (Leica Stellaris STED). Cytotoxicity of the nanoparticles (dye loaded and unloaded) was then evaluated with a CyQUANT LDH Cytotoxicity Assay Kit (Invitrogen) using a microplate reader BioTek Synergy H1. HSD test was performed to calculate differences in viability between loaded and unloaded particles at different concentrations.

Hemolysis Assay: Hemolysis was performed according to previously published protocols.[66–68] Briefly, P(Bz_HF_5), P(Bz_HF_10), and P(Bz_HF_20) NPs in 1x PBS pH 7.4. were combined with washed and isolated BALB/c red blood stocks (1:50 dilution from originally concentrated fraction from 250 µL of K2-EDTA treated whole blood) at a 1:10 (v/v) ratio in quadruplicate in a 96 clear-well COSTAR plate (final volume 200 uL well^{-1}). At a final treatment concentration of 0.125 mg mL^{-1}, the samples were then incubated for 1 h at 37 °C, and then centrifuged at 4 °C for 10 min at 500xg. 100 µL of supernatant was collected to measure peak hemolytic absorbance in quadruplicate at 405 nm by UV–vis/fluorescent plate-reader (BioTek Synergy H1, Serial No. 19 012 817). 20% Triton X-100 and 1x PBS pH 7.4 were used as positive and negative internal controls at the same treatment dilution. The 1x PBS negative control was subtracted as a minimum baseline (0%) from all samples, and the Triton-X-100 positive control was used as a maximum baseline (100%) to calculate normalized hemolytic percentages with standard error of mean (n = 4). A one-way ANOVA was used to determine significant differences across all three treatment groups, while a paired two-tail t-test of means was used to determine significance between 2 samples at a time.

Supporting Information

Supporting Information is available from the Wiley Online Library or from the author.

Acknowledgements

A.K. and M.L.Y. contributed equally to this work. D.L.W. and A.K. thank the National Science Foundation (2235617, CHEM-MSN) for funding. E.E.L.T. and C.M.H. acknowledges the PhRMA Foundation, the National Science Foundation (2236629 and 1757220), the National Institutes of Health (1R01EB034086), and the College of Liberal Arts at the University of Mississippi for funding. A.S.F. would like to thank Mississippi INBRE (P20GM103476). E.L.Q. and D.J.C. thank the Welch Foundation (F-1883) and a UT Austin Provost's Graduate Excellence Fellowship.

Conflict of Interest

The authors declare no conflict of interest.

Data Availability Statement

The data that support the findings of this study are available in the supplementary material of this article.

Keywords

magnetic resonance imaging (MRI), nanoparticles, polymers, reversible addition-fragmentation chain transfer (RAFT), self-assembly

Received: September 21, 2024
Revised: November 1, 2024
Published online:

[1] I. Tirotta, V. Dichiarante, C. Pigliacelli, G. Cavallo, G. Terraneo, F. B. Bombelli, P. Metrangolo, G. Resnati, *Chem. Rev.* **2015**, *115*, 1106.
[2] S. M. Hosseini, J. Mohammadnejad, S. Salamat, Z. Beiram Zadeh, M. Tanhaei, S. Ramakrishna, *Mater. Today. Chem.* **2023**, *29*, 101400.
[3] S. Shuvaev, E. Akam, P. Caravan, *Invest. Radiol.* **2021**, *56*, 20.
[4] A. Gupta, P. Caravan, W. S. Price, C. Platas-Iglesias, E. M. Gale, *Inorg. Chem.* **2020**, *59*, 6648.
[5] G. J. Soufi, A. Hekmatnia, S. Iravani, R. S. Varma, *ACS Appl. Nano. Mater.* **2022**, *5*, 10151.
[6] A. L. Lee, A. K. Pandey, S. Chiniforoush, M. Mandal, J. Li, C. J. Cramer, C. L. Haynes, W. C. K. Pomerantz, *Anal. Chem.* **2022**, *94*, 3782.
[7] N. Łopuszyńska, K. Szczepanowicz, K. Jasiński, P. Warszyński, W. P. Węglarz, *Nanomaterials* **2020**, *10*, 2127.
[8] O. Diou, N. Tsapis, C. Giraudeau, J. Valette, C. Gueutin, F. Bourasset, S. Zanna, C. Vauthier, E. Fattal, *Biomater* **2012**, *33*, 5593.
[9] J.-X. Yu, R. R. Hallac, S. Chiguru, R. P. Mason, *Prog. Nucl. Magn. Reson. Spectrosc.* **2013**, *70*, 25.
[10] C. Fu, S. Herbst, C. Zhang, A. K. Whittaker, *Polym. Chem.* **2017**, *8*, 4585.
[11] M. Rosati, A. Acocella, A. Pizzi, G. Turtù, G. Neri, N. Demitri, Nonappa, G. R., B. Donnio, F. Zerbetto, F. B. Bombelli, G. Cavallo, P. Metrangolo, *Macromolecules* **2022**, *55*, 2486.
[12] K. Wang, H. Peng, K. J. Thurecht, S. Puttick, A. K. Whittaker, *Polym. Chem.* **2013**, *4*, 4480.
[13] V. M. Panakkal, D. Havlicek, E. Pavlova, M. Filipová, S. Bener, D. Jirak, O. Sedlacek, *Biomacromolecules* **2022**, *23*, 4814.
[14] R. Holman, O. Lorton, P. C. Guillemin, S. Desgranges, C. Contino-Pépin, R. Salomir, *Front. Chem.* **2022**, *9*, https://doi.org/10.3389/fchem.2021.810029.
[15] V. Lau, L. Xiao, Y. Zhao, S. Su, Y. Ding, C. Man, X. Wang, A. Tsang, P. Cao, G. K. K. Lau, G. K. K. Leung, A. T. L. Leong, E. X. Wu, *Magn. Reson. Med.* **2023**, *90*, 400.
[16] U. Nayanathara, B. R. Herling, N. Ansari, C. Zhang, S. R. Logan, M. A. Beach, S. A. Smith, N. R. B. Boase, A. P. R. Johnston, G. K. Such, *ACS Appl. Nano Mater.* **2023**, *6*, 10015.
[17] A. K. Pearce, A. B. Anane-Adjei, R. J. Cavanagh, P. F. Monteiro, T. M. Bennett, V. Taresco, P. A. Clarke, A. A. Ritchie, M. R. Alexander, A. M. Grabowska, C. Alexander, *Adv. Healthcare. Mater.* **2020**, *9*, 2000892.
[18] B. A. Aguilar-Castillo, J. L. Santos, H. Luo, Y. E. Aguirre-Chagala, T. Palacios-Hernández, M. Herrera-Alonso, *Soft Matter* **2015**, *11*, 7296.
[19] S. E. Kirberger, S. D. Maltseva, J. C. Manulik, S. A. Einstein, B. P. Weegman, M. Garwood, W. C. K. Pomerantz, *Angew. Chem., Int. Ed.* **2017**, *56*, 6440.
[20] C. Fu, J. Tang, A. Pye, T. Liu, C. Zhang, X. Tan, F. Han, H. Peng, A. K. Whittaker, *Biomacromolecules* **2019**, *20*, 2043.
[21] K. Wang, H. Peng, K. J. Thurecht, S. Puttick, A. K. Whittaker, *Polym. Chem.* **2014**, *5*, 1760.
[22] J. Li, S. E. Kirberger, Y. Wang, H. Cui, C. R. Wagner, W. C. K. Pomerantz, *Bioconjug. Chem.* **2023**, *34*, 1477.
[23] S.-P. Wen, Q. Yue, L. A. Fielding, *Polym. Chem.* **2021**, *12*, 2122.
[24] T. P. Lodge, M. Muthukumar, *J. Phys. Chem.* **1996**, *100*, 13275.
[25] A. A. Cockram, T. J. Neal, M. J. Derry, O. O. Mykhaylyk, N. S. J. Williams, M. W. Murray, S. N. Emmett, S. P. Armes, *Macromolecules* **2017**, *50*, 796.
[26] M. J. Rymaruk, C. T. O'Brien, S. L. Brown, C. N. Williams, S. P. Armes, *Macromolecules* **2020**, *53*, 1785.
[27] S. Boner, K. Parkatzidis, N. D. A. Watuthanthrige, A. Anastasaki, *Eur. Polym. J.* **2024**, *205*, 112721.
[28] C. D. Wood, K. Senoo, C. Martin, J. Cuellar, A. I. Cooper, *Macromolecules* **2002**, *35*, 6743.
[29] M. Khan, T. R. Guimarães, K. Choong, G. Moad, S. Perrier, P. B. Zetterlund, *Macromolecules* **2021**, *54*, 736.
[30] E. R. Jones, M. Semsarilar, A. Blanazs, S. P. Armes, *Macromolecules* **2012**, *45*, 5091.
[31] T. R. Guimarães, Y. L. Bong, S. W. Thompson, G. Moad, S. Perrier, P. B. Zetterlund, *Polym. Chem.* **2021**, *12*, 122.
[32] A. Grigoreva, A. Vihireva, S. Zaitsev, *Polym. Bull.* **2024**, *81*, 8701.
[33] M. Machtakova, H. Thérien-Aubin, K. Landfester, *Chem. Soc. Rev.* **2022**, *51*, 128.
[34] K. Kuperkar, L. I. Atanase, A. Bahadur, I. C. Crivei, P. Bahadur, *Polymers* **2024**, *16*, 206.
[35] C. L. Zhao, M. A. Winnik, G. Riess, M. D. Croucher, *Langmuir* **1990**, *6*, 514.
[36] M. L. Yaddehige, I. Chandrasiri, A. Barker, A. K. Kotha, J. S. Dal Williams, B. Simms, P. Kucheryavy, D. G. Abebe, M. B. Chougule, D. L. Watkins, *ChemNanoMat* **2020**, *6*, 1833.
[37] Z. Su, Y. Takeda, D. Matsui, Y. Toyotake, M. Wakayama, *Colloid Polym. Sci.* **2024**, *302*, 1123.
[38] N. J. Turro, A. Yekta, *J. Am. Chem. Soc.* **1978**, *100*, 5951.
[39] K. N. Clayton, J. W. Salameh, S. T. Wereley, T. L. Kinzer-Ursem, *Biomicrofluidics* **2016**, *10*, 054107.
[40] S. Mazumdar, D. Chitkara, A. Mittal, *Acta Pharm. Sin. B.* **2021**, *11*, 903.
[41] J. M. Morachis, E. A. Mahmoud, A. Almutairi, *Pharmacol. Rev.* **2012**, *64*, 505.
[42] J. W. Hickey, J. L. Santos, J. M. Williford, H. Q. Mao, *J. Contr. Release* **2015**, *219*, 536.
[43] S. Behzadi, V. Serpooshan, W. Tao, M. A. Hamaly, M. Y. Alkawareek, E. C. Dreaden, D. Brown, A. M. Alkilany, O. C. Farokhzad, M. Mahmoudi, *Chem. Soc. Rev.* **2017**, *46*, 4218.
[44] B. Yameen, W. I. Choi, C. Vilos, A. Swami, J. Shi, O. C. Farokhzad, *J. Controlled. Release.* **2014**, *190*, 485.
[45] L. Evensen, P. L. Johansen, G. Koster, K. Zhu, L. Herfindal, M. Speth, F. Fenaroli, J. Hildahl, S. Bagherifam, C. Tulotta, L. Prasmickaite, G. M. Mælandsmo, E. Snaar-Jagalska, G. Griffiths, *Nanoscale* **2016**, *8*, 862.
[46] X.-R. Shao, X.-Q. Wei, X. Song, L.-Y. Hao, X.-X. Cai, Z.-R. Zhang, Q. Peng, Y.-F. Lin, *Cell. Prolif.* **2015**, *48*, 465.
[47] J. Bar, S. Spencer, S. Morgan, L. Brooks, D. Cunningham, J. Robertson, J. M. Jürgensmeier, G. D. Goss, *Clin. Colorectal. Cancer.* **2014**, *13*, 46.
[48] K. J. Thurecht, I. Blakey, H. Peng, O. Squires, S. Hsu, C. Alexander, A. K. Whittaker, *J. Am. Chem. Soc.* **2010**, *132*, 5336.
[49] X. Wang, S. Guo, Z. Li, Q. Luo, Y. Dai, H. Zhang, Y. Ye, Q. Gong, K. Luo, *J. Nanobiotechnology* **2021**, *19*, 205.
[50] L. J. Scott, *Clin. Drug. Investig.* **2018**, *38*, 773.
[51] C. Fu, C. Zhang, H. Peng, F. Han, C. Baker, Y. Wu, H. Ta, A. K. Whittaker, *Macromolecules* **2018**, *51*, 5875.
[52] Y. Wang, X. Tan, A. Usman, Y. Zhang, M. Sawczyk, P. Král, C. Zhang, A. K. Whittaker, *ACS Macro Lett.* **2022**, *11*, 1195.
[53] I. Chandrasiri, M. Loku Yaddehige, B. Li, Y. Sun, W. E. Meador, A. Dorris, M. Farid Zia, N. I. Hammer, A. Flynt, J. H. Delcamp, E. Davis, A. Lippert, D. L. Watkins, *ACS Appl. Polym. Mater.* **2022**, *4*, 2972.
[54] I. Chandrasiri, D. G. Abebe, M. Loku Yaddehige, J. S. D. Williams, M. F. Zia, A. Dorris, A. Barker, B. L. Simms, A. Parker, B. P. Vinjamuri, N. Le, J. N. Gayton, M. B. Chougule, N. I. Hammer, A. Flynt, J. H. Delcamp, D. L. Watkins, *ACS Appl. Bio Mater.* **2020**, *3*, 5664.
[55] W. Zhao, M. Zeng, K. Li, C. Pi, Z. Liu, C. Zhan, J. Yuan, Z. Su, Y. Wei, J. Wen, F. Pi, X. Song, R. J. Lee, Y. Wei, L. Zhao, *Pharm. Biol.* **2022**, *60*, 2300.
[56] G. Yang, Y. Liu, S. Jin, Y. Hui, X. Wang, L. Xu, D. Chen, D. Weitz, C.-X. Zhao, *Aggregate* **2023**, *4*, e314.
[57] Y. Liu, G. Yang, T. Baby, Tengjisi, D. C., D. A. Weitz, C.-X. Zhao, *Angew. Chem., Int. Ed.* **2020**, *59*, 4720.
[58] J. L. Van der Velden, I. Bertoncello, J. L. McQualter, *Respir. Res.* **2013**, *14*, 123.

[59] T. Balbi, C. Ciacci, L. Canesi, *Comp. Biochem. Physiol. C.* **2019**, *222*, 135.
[60] L. Gatti, C. Chirizzi, G. Rotta, P. Milesi, M. Sancho-Albero, V. Sebastián, A. Mondino, J. Santamaría, P. Metrangolo, L. Chaabane, F. B. Bombelli, *Nanoscale. Adv.* **2023**, *5*, 3749.
[61] G. Sicilia, A. L. Davis, S. G. Spain, J. P. Magnusson, N. R. B. Boase, K. J. Thurecht, C. Alexander, *Polym. Chem.* **2016**, *7*, 2180.
[62] T. A. Ranathunge, M. L. Yaddehige, J. H. Varma, C. Smith, J. Nguyen, I. Owolabi, W. Kolodziejczyk, N. I. Hammer, G. Hill, A. Flynt, D. L. Watkins, *Front. Chem.* **2021**, *9*, 729125.
[63] S. Stefanovic, K. McCormick, S. Fattah, R. Brannigan, S.-A. Cryan, A. Heise, *Polym. Chem.* **2023**, *14*, 3151.
[64] J. R. Góis, A. V. Popov, T. Guliashvili, A. C. Serra, J. F. J. Coelho, *RSC Adv.* **2015**, *5*, 91225.
[65] H. Namazi, S. Jafarirad, *J. Pharm. Sci.* **2011**, *14*, 162.
[66] C. M. Hamadani, I. Chandrasiri, M. L. Yaddehige, G. S. Dasanayake, I. Owolabi, A. Flynt, M. Hossain, L. Liberman, T. P. Lodge, T. A. Werfel, D. L. Watkins, E. E. L. Tanner, *Nanoscale* **2022**, *14*, 6021.
[67] C. M. Hamadani, M. J. Goetz, S. Mitragotri, E. E. L. Tanner, *Sci. Adv.* **2020**, *6*, 48.
[68] C. M. Hamadani, G. S. Dasanayake, M. E. Gorniak, M. C. Pride, W. Monroe, C. M. Chism, R. Heintz, E. Jarrett, G. Singh, S. X. Edgecomb, E. E. L. Tanner, *Nat. Protoc.* **2023**, *18*, 2509.